Stable orthorhombic ferroelectric Hf$_{0.5}$Zr$_{0.5}$O$_2$ films with platinum seed electrodes grown by sputtering 🄵

Jiang Zhu 🄳 ; Yongyi Wu 🄳 ; Hao-Nan Li; Lei Wang; Yue-Qi Wang 🄳 ; Xian-Qin Liu; Yi-Xing He; Siwen Zhang; Jie Su 🄳 ; Tao Li 🄳 ; Haijiao Harsan Ma ✉ 🄳 ; Jincheng Zhang; Yue Hao 🄳

Check for updates

View Online   Export Citation

Articles You May Be Interested In

Determination of the density of the defect states in Hf$_{0.5}$Zr$_{0.5}$O$_2$ high-k film Deposited by using rf-magnetron sputtering technique

AIP Advances (August 2014)

Interface effects in the phase determination of Hf$_{0.5}$Zr$_{0.5}$O$_2$ epitaxial thin films

APL Mater. (January 2025)

Grain size engineering for ferroelectric Hf$_{0.5}$Zr$_{0.5}$O$_2$ films by an insertion of Al$_2$O$_3$ interlayer

Appl. Phys. Lett. (November 2014)

Stable orthorhombic ferroelectric Hf$_{0.5}$Zr$_{0.5}$O$_2$ films with platinum seed electrodes grown by sputtering Ⓕ

View Online   Export Citation   CrossMark

Jiang Zhu,[1,2,3] ⓘ Yongyi Wu,[4] ⓘ Hao-Nan Li,[1,2,3] Lei Wang,[1,2,3] Yue-Qi Wang,[1,2,3] ⓘ Xian-Qin Liu,[1,2,3]
Yi-Xing He,[1,2,3] Siwen Zhang,[1,2,3] Jie Su,[2,3] ⓘ Tao Li,[4] ⓘ Haijiao Harsan Ma,[1,2,3,5,a)] ⓘ Jincheng Zhang,[1,2,3,5]
and Yue Hao[1,2,3,5] ⓘ

AFFILIATIONS

[1] State Key Laboratory of Wide Bandgap Semiconductor Devices and Integrated Technology, Xidian University,
2 South Taibai Road, Xi'an 710071, China
[2] Low Dimensional Quantum Physics and Device Group, School of Microelectronics, Xidian University, 2 South Taibai Road,
Xi'an 710071, China
[3] State Key Discipline Laboratory of Wide Band Gap Semiconductor Technology, School of Microelectronics, Xidian University,
2 South Taibai Road, Xi'an 710071, China
[4] Center for Spintronics and Quantum Systems, State Key Laboratory for Mechanical Behavior of Materials,
Department of Materials Science and Engineering, Xi'an Jiaotong University, Xi'an 710049, China
[5] Collaborative Innovation Center of Quantum Information of Shaanxi Province, Xidian University, Xi'an 710071, China

[a)] Author to whom correspondence should be addressed: mahj07@xidian.edu.cn

ABSTRACT

High quality ferroelectric Hf$_{0.5}$Zr$_{0.5}$O$_2$ films are crucial for next generation nanoelectronics. However, the growth of large-sized stable ferroelectric Hf$_{0.5}$Zr$_{0.5}$O$_2$ films is challenging. Here, we demonstrate the synthesis of large-sized stable orthorhombic ferroelectric Hf$_{0.5}$Zr$_{0.5}$O$_2$ thin films through the use of a (111)-oriented platinum electrode acting as a seed template. Pt(111) is chosen as a seed layer to grow HfO$_2$ and Hf$_{0.5}$Zr$_{0.5}$O$_2$ layers on top of it using physical vapor deposition. High-quality monoclinic HfO$_2$ is obtained and verified by X-ray diffraction (XRD) and transmission electron microscopy (TEM). We further obtained orthorhombic phase Hf$_{0.5}$Zr$_{0.5}$O$_2$ on MgO and sapphire substrates with Pt seed layers, characterized by XRD, scanning TEM, and selective area diffraction. The Hf$_{0.5}$Zr$_{0.5}$O$_2$ thin films show robust and switchable ferroelectric polarization. Thermodynamic analyses reveal the role of nucleation and surface energy in stabilizing the polar orthorhombic phase and the non-polar-monoclinic phase along different directions. The strain due to the lattice and thermal expansion coefficient mismatch is crucial for stabilizing the stable orthorhombic ferroelectric Hf$_{0.5}$Zr$_{0.5}$O$_2$ films.

INTRODUCTION

Hafnia-based ferroelectric materials have attracted great attention due to their robust and scalable ferroelectricity at nanoscale thickness and compatibility with conventional silicon-based semiconductor technology, making them promising candidates for non-volatile memory and ferroelectric transistors.[1–7] There has been abundant research on the chemical and interfacial engineering of hafnia-based ferroelectrics, particularly in polycrystalline films grown using atomic-layer deposition (ALD).[8–15] The process of stabilizing the ferroelectric metastable orthorhombic phase is usually recognized as the dominant ferroelectric phase in Hf$_{1-x}$Zr$_x$O$_2$ films. Rapid thermal annealing in ALD-grown films is crucial.[16–19] It has been realized that the orientation of both the substrate and seed layer is one key factor influencing the formation and growth of the metastable ferroelectric phases in Hf$_{1-x}$Zr$_x$O$_2$.[15] The stable

22 September 2025 07:00:13

monoclinic phase structure is not desirable for achieving high-quality ferroelectric $Hf_{1-x}Zr_xO_2$ films, in which non-ferroelectric tetragonal and monoclinic phases inevitably coexist with ferroelectric orthorhombic phases and weaken the ferroelectricity of the film.[20–22] It has been a challenge to directly grow and stabilize ferroelectric orthorhombic $Hf_{1-x}Zr_xO_2$ films with minimized non-ferroelectric phases with physical vapor deposition or ALD.[17,19,23,24]

HfO_2 has a non-polar tetragonal/cubic structure at high temperatures (>500 °C) and stabilizes to a monoclinic structure when temperature is reduced to room temperature.[25–27] HfO_2 could also be stabilized with an orthorhombic structure via external pressure, doping, or strain. The stable growth of orthorhombic $Hf_{0.5}Zr_{0.5}O_2$ (HZO) films was successfully achieved by ALD with rapid thermal crystallization on Si(001) and Si(111) substrates.[28–30]

Recently, epitaxial ferroelectric HZO films have been successfully fabricated using pulsed laser deposition with metallic oxide buffer electrodes such as $La_{1-x}Sr_xMnO_3$ on $SrTiO_3(100)(110)$ (111)[31] and $Pb_2Ir_2O_7$ on yttria-stabilized zirconia (YSZ) substrates[32] and $LaNiO_3$, $SrRuO_3$.[33,34] $La_{1-x}Sr_xMnO_3$ and $Pb_2Ir_2O_7$ act as seed electrode layers and structure templates for the stable growth of orthorhombic or rhombohedral $Hf_{1-x}Zr_xO_2$. In these cases, a high quality stable oxide seed electrode is a must and requires special growth techniques, typically pulsed laser deposition, which might be expensive and high cost. However, fabricating stable single-crystal HZO thin films, especially at wafer scale, poses its own challenges as well.[18,29] The fabrication of HZO single crystals is a

sophisticated and demanding process, heavily influenced by various factors including material properties, crystal growth kinetics, and crystal structure control.[32,34] Throughout the growth phase, precise regulation of parameters such as temperature, pressure, and solution composition is imperative to ensure the crystal attains superior quality and uniformity. Furthermore, managing impurities and defects presents a formidable challenge in the fabrication process, necessitating refinement through meticulous experimental design and post-processing methodologies.[26,35] To achieve large-size uniform stable ferroelectric HZO film growth on different substrates, especially widely used silicon and sapphire, with simple seed template material and relatively low cost is highly desirable for next generation nonvolatile memory and ferroelectric transistors.

Here, we demonstrate the growth of large size high-quality monoclinic phase (m-phase) HfO_2 and ferroelectric stable orthorhombic phase (o-phase) dominated HZO using a simple platinum metal electrode as a seed layer via physical vapor deposition. The platinum metal electrodes along the (111) direction play a structural template role and induce high quality (111)-orientation preferred HZO growth. Monoclinic HfO_2 and orthorhombic HZO films can be realized on sapphire and MgO substrates by inserting a Pt seed layer. The orthorhombic phase HZO could be dominated by increasing the growth temperature above 500 °C. Uniform ferroelectricity can be achieved for HZO thin films grown on sapphire and MgO substrates by using a Pt(111) seed layer. We performed theoretical analysis to reveal the dynamical mechanisms of the formation of monoclinic and orthorhombic HZO films along (001),
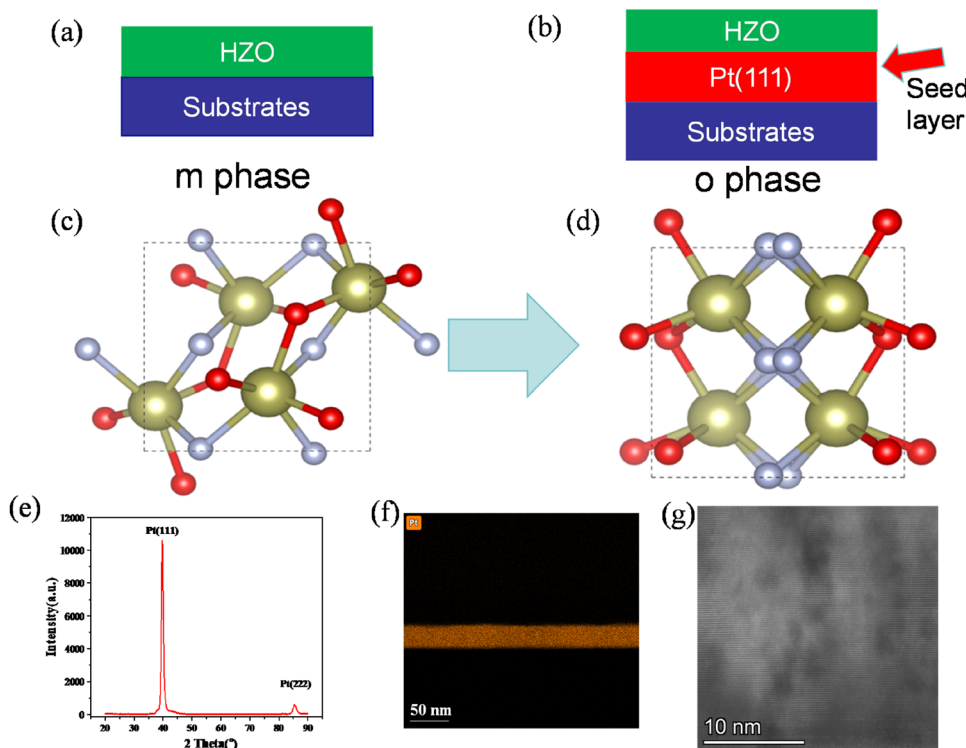
FIG. 1. (111)-oriented o-phase HZO induced by Pt(111) seed layer. m-phase HZO is formed without the insertion of the Pt seed layer. (a) Schematic structure of the monoclinic HZO on the substrate. (b) Schematic structure of the induced orthorhombic HZO on a substrate with Pt seed layer. (c) Atomic crystal structure of m phase HZO. (d) Atomic crystal structure of o-phase HZO. (e) The out-of-plane x-ray θ–2θ scan of the Pt(111) seed layer. (f) Energy dispersive x-ray spectroscopy mapping of Pt seed layer. (g) High-resolution transmission electron microscopy of Pt(111) films.

(100), and (111) directions, taking into account the nucleation and surface energy.

The seed layer can improve the selective orientation of the film growth process, reduce the grain size, change the grain spacing of the film, and improve the densification, uniformity, and crystallinity of the film. Furthermore, the seed layer plays the role of a buffer layer to improve the contact between the substrate and the film and optimize the lattice match between the film and the substrate, which is precisely what we have utilized in the present work (Fig. 1). The chosen seed layer has to be easy to grow and has an ideal lattice structure for the HZO films, in which the crystal structure transforms from m-phase to o-phase. A natural choice is to utilize a cubic Pt layer with (111)-orientation. The introduction of the Pt seed layer along the (111) direction was used to obtain high-quality monoclinic HfO_2 and orthorhombic HZO films. The substrates used are sapphire Al_2O_3(11-20) and MgO(001) substrates. The inserted Pt seed layer is (111)-orientation texture dominated, with a (111) peak at 39.7° and a (222) peak at 85.6° in X-ray diffraction (XRD) as observed in Fig. 1(e). Energy dispersive x-ray spectroscopy mapping of the Pt seed layer shown in Fig. 1(f) and high-resolution transmission electron microscopy (TEM) of Pt(111) films in Fig. 1(g) show the high quality of the Pt seed layer. We analyzed the scanning TEM (STEM) images of the Pt film. By performing a Fourier transform on the STEM image of the rectangular region of the film, we obtained lattice fringes (Fig. S5). As shown in Fig. S5, the lattice fringes are well-ordered and of uniform size. We determined the lattice constant of the Pt film to be 0.382 nm, with an error of 1.7% compared to the well-known Pt lattice constant. In addition, the XRD results show peaks corresponding to both the (111) and (222) orientations in Fig. 1(e), indicating that the Pt film is a high-quality epitaxial layer.

Figure 2 shows the crucial role of the insertion of the Pt seed layer. A very strong monoclinic peak (red solid line) of HfO_2 appears when the seed layer Pt was introduced, as shown in Fig. 2(a), in which a peak around 28.4° corresponds to the (1-11) peak of monoclinic HfO_2. In comparison, no such peak appears (black solid line) that could be obtained for HfO_2 directly grown on a sapphire substrate. This indicates that the seed Pt layer improves the contact between the substrate and the film and the stable thin film of HfO_2 film. Figure 2(b) shows the cross section transmission electron microscopy (TEM) image of the obtained HfO_2 film with a Pt insertion seed layer on a sapphire substrate, showing clear contrast at the interfaces. The thickness of the HfO_2 film is 15 nm, indicated with green lines. The bottom Pt insertion layer shows a brighter view in the cross section TEM image. The high-resolution TEM image [Fig. 2(c)] shows high crystallinity of the HfO_2 film grown by physical vapor deposition. We further show high-resolution scanning transmission electron microscopy (STEM) with atomic resolution in Fig. 2(d). The results show that the monoclinic phase of the HfO_2 film is well arranged, and the quality of the film at atomic resolution is high. The extracted interatomic distance of HfO_2 is ~0.316 nm. These results show that the insertion of a (111)-textured Pt seed layer can induce stable m-phase HfO_2 growth.

To further demonstrate the role of the Pt seed layer, we grow HZO films on sapphire and MgO substrates as a function of thickness with different growth temperatures. HZO is an alloy in which Zr is used as a dopant to stabilize ferroelectric HfO_2-based thin films. Due to the physical similarity between HfO_2 and ZrO_2, both of which are fluorite in structure, and the similarity in chemical properties brought about by having the same electronic structure, which makes Zr as a dopant highly compatible with the Hf-based thin films. HZO films are directly sputtered using a HZO ceramic target. Similar to the growth of m-phase HfO_2, Pt(111) is introduced as a seed layer in the growth of HZO. Figure 3 shows the characterization of HZO films grown with the Pt seed layer. Thickness-dependent x-ray θ–2θ scan of the HZO films with a Pt seed layer on sapphire
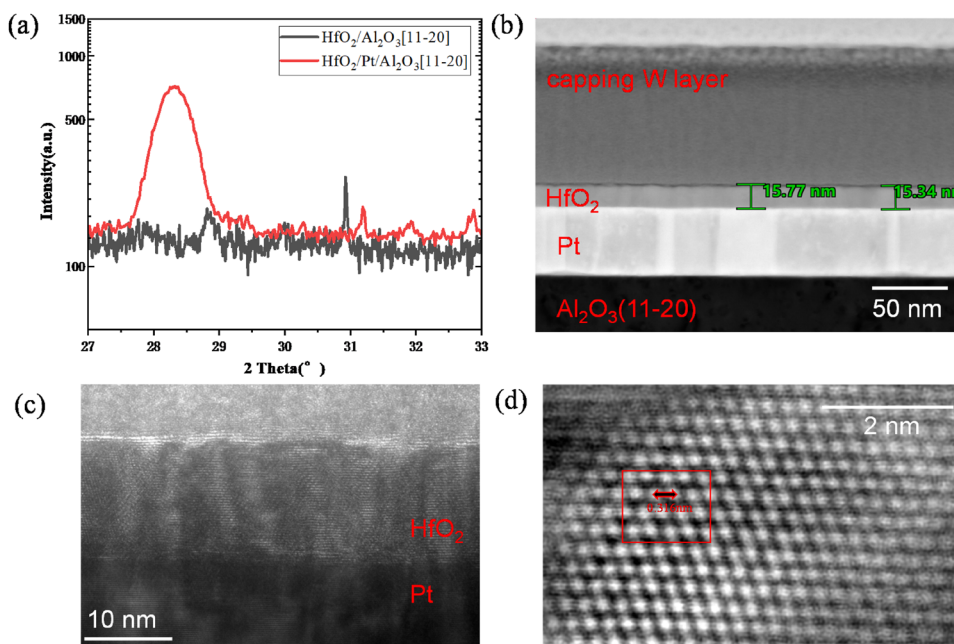
FIG. 2. Monoclinic HfO_2 grown on Al_2O_3(11–20) with a (111)-orientated Pt insertion layer. (a) The out-of-plane x-ray θ–2θ scan of the 15 nm HfO_2 film on sapphire showing the m-phase peak with/without the Pt seed layer. The dark line shows the XRD of HfO_2 film as grown on the substrate, and the red line shows the XRD of monoclinic HfO_2 on the substrate with the Pt(111) seed layer. (b) Cross section transmission electron microscopy (TEM) of a 15 nm HfO_2 film on 50 nm Pt(111) on sapphire. (c) High resolution TEM shown in (b). (d) Scanning TEM (STEM) of HfO_2 film shown (c) with atomic resolution, and the interatomic distance of HfO_2 films on sapphire is 0.316 nm.
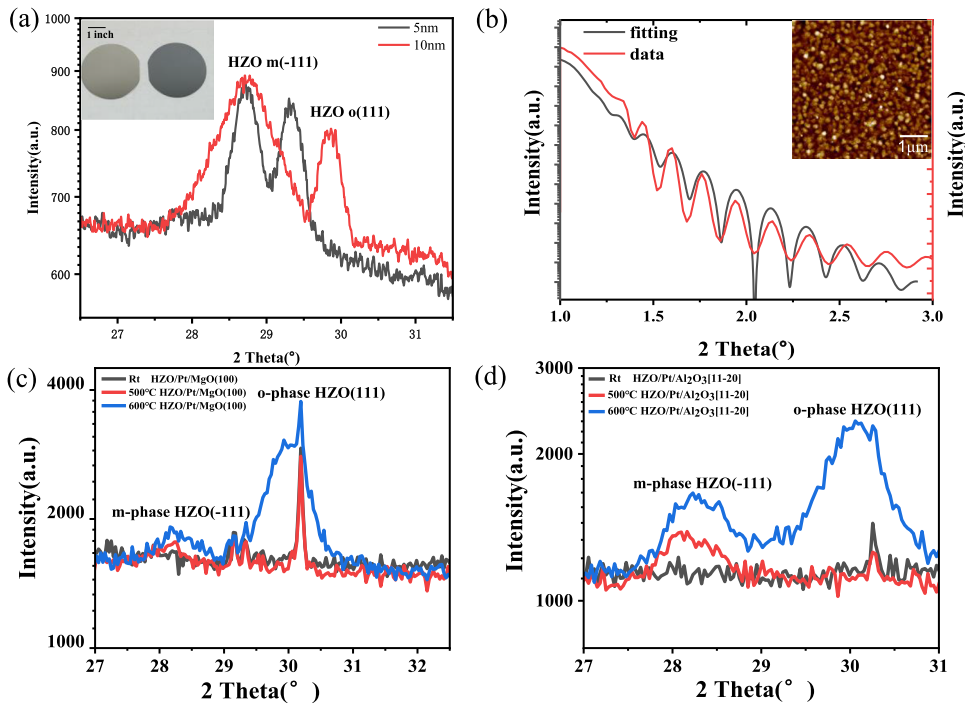
FIG. 3. Characterization of HZO thin films with varying temperature and thickness using XRD and XRR. (a) Thickness dependent out-of-plane x-ray $\theta-2\theta$ scan of the HZO films on sapphire grown with Pt seed layer. The inset shows an optical photograph of 20 nm HZ0 on a 2-in. silicon wafer with a Pt seed layer. (b) Comparison between experimental x-ray reflectivity curve and software fitting curve. The inset shows an atomic force microscopy image of a 20 nm HZO film. (c) Temperature dependent out-of-plane x-ray $\theta-2\theta$ scan of the 20 nm-HZO film on MgO(100) grown with a Pt seed layer. (d) Temperature dependent out-of-plane x-ray $\theta-2\theta$ scan of the HZO film on Al_2O_3(11–20) grown with a Pt seed layer.

substrates is shown in Fig. 3(a). In Fig. 3(a), it can be observed that when the thickness is 10 nm, a HZO o-phase peak at around 30° is displayed, while at 5 nm, a peak at around 29° is observed. We believe this is an intermediate state of transition from m-phase to o-phase during the growth process. We note that the monoclinic m(-111) phase near 28.5° can be clearly obtained when no Pt seed layer is introduced (Fig. S1), and an orthorhombic o(111) phase at 30.2° has been significantly enhanced after the introduction of the Pt(111) seed layer. The left panel of the inset in Fig. 3(a) illustrates the growth of the HZO/Pt thin film on a 2-in. silicon wafer, while the right shows an image of the 2-in. silicon wafer, showing the contrast without HZO/Pt films. Due to the white or transparent nature of HZO, the thick HZO film in the left image exhibits a macroscopic appearance of the silver-white color of Pt. The thickness of 5 nm HZO films is characterized by X-ray reflectivity (XRR) as shown in Fig. 3(b). The XRR curve represents a feature of the HZO/Pt bilayer structure. We constructed a bilayer model consisting of a 5 nm HZO and a 35 nm Pt layer and simulated the XRR curve as shown in Fig. 3(b), which fits well with the experimental data in Fig. S2. Considering factors such as roughness, it can be calculated that the actual thickness of the HZO film is ~5 nm as estimated. As demonstrated in the inset in Fig. 3(b), the atomic force microscopy image shows good surface quality with a roughness of 1.26 nm for the 20 nm HZO film on sapphire.

TEM images and high-resolution STEM data shown in Figs. 4(a) and 4(b) of the HZO film grown on a sapphire substrate with a Pt seed layer show that the HZO films are quasi-epitaxial. A stable HZO film was formed, which may be a mixed phase of orthorhombic and tetragonal phases. Combined with the fact of the XRD peak near 30°, we refer to the mixed phase as being

dominated by orthorhombic phases and having high-quality thin films at atomic resolution. Figure 4(a) shows a high resolution TEM image of a 20 nm HZO on a Pt(111) seed layer. The interatomic distance on $Hf_{0.5}Zr_{0.5}O_2$ films on sapphire is 0.29 nm, as shown in Fig. 4(b), which is very consistent with the interatomic distance of the orthogonal ferroelectric o-phase in the HZO films mentioned in the literature.[36] Simultaneously, to further investigate the internal structure of the crystal, we performed Selective Area Diffraction (SAD) of the HZO film grown on sapphire. Figure 4(c) shows a SAD image of the HZO film with a thickness of 10 nm, while Fig. 4(d) showcases a SAD image of the HZO film with a thickness of 20 nm. The analysis of SAD data of the 10 nm-thin sample in Fig. 4(c) indicates a stable growth of the HZO film. The central bright spot represents the transmission spot, while the three diffraction spots adjacent to it collectively form a parallelogram. This configuration signifies the smallest plane within the crystal lattice.[35] Utilizing software, we meticulously examined the distance and angular relationships between two points and compared them with the theoretical values of HZO. Remarkably, nearly every point within the plane correlates with a crystal plane exhibiting the o-phase orientation. This compellingly suggests that the HZO thin film of about 10 nm manifests as a high-quality stable film. Applying the same analytical approach to Fig. 4(d), we can also discern three distinct orientations of the o-phase. However, there are noticeable diffraction spots in the image that do not align with this plane. Due to the limited area selected, determining the specific plane is challenging, thus impeding a detailed analysis of the crystal structure. Concerning the XRD data shown in Fig. 3, we could come to the conclusion that these diffraction spots most likely belong to the m-phase. Combining these findings, we infer that sputtering a seed layer induces
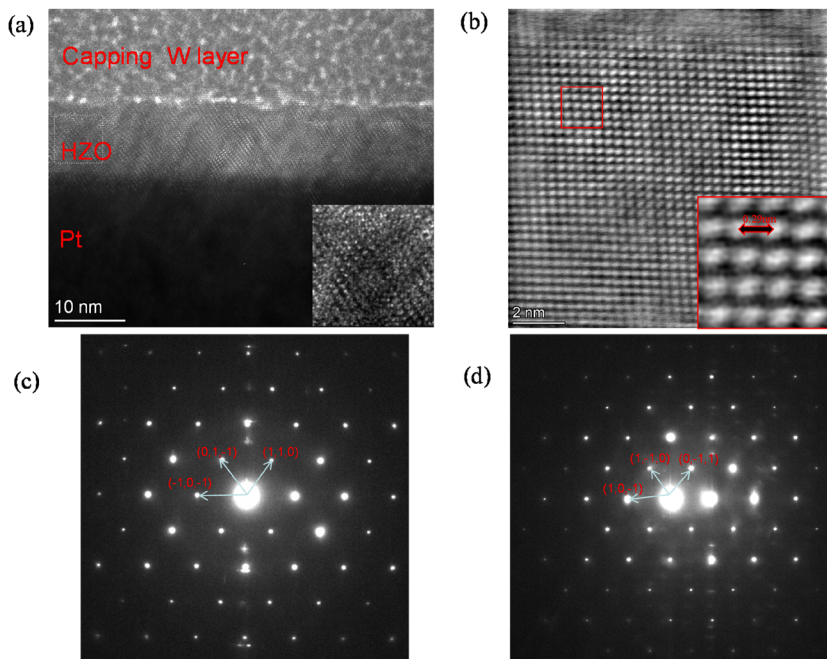
FIG. 4. TEM image and selective area diffraction (SAD) of stable orthorhombic HZO grown on Al_2O_3(11–20) substrate with (111)-oriented Pt seed layer. (a) High-resolution TEM image of a 20 nm HZO on Pt(111) seed layer. (b) Scanning TEM (STEM) of HZO film shown (c) with atomic resolution, and the interatomic distance of $Hf_{0.5}Zr_{0.5}O_2$ films on sapphire is 0.29 nm. (c) The SAD diffraction pattern of 10 nm HZO grown on Al_2O_3(11-20) substrate with a (111)-oriented Pt seed layer. (d) The SAD diffraction pattern of 20 nm HZO grown on Al_2O_3(11-20) substrate with (111)-oriented Pt seed layer.

stable growth of high quality o-phase HZO thin films, with the potential to modulate HZO crystal phases by adjusting thickness.

We notice that the proportion of the orthorhombic phase strongly depends on the growth temperature as well as the substrate [Figs. 3(c) and 3(d)]. The intensity of the orthorhombic phase is much stronger than that of the monoclinic phase when the growth temperature is 600 °C, indicating different formation energy of the m-phase and o-phase. This is consistent with the conclusion that the transition/formation temperature of the orthorhombic phase of HZO is about 550 °C.[35] A further increase of temperature to 700 °C would lead to an enhancement of the XRD peak intensity of the o-phase; however, it also hugely increases the roughness of the deposited films and damages the surface quality of the sample (Fig. S3). Therefore, we choose 600 °C as the best condition for the deposition of the HZO films. The portion of o-phase HZO and m-phase HZO varied with the thickness of the functional layer HZO. We also notice that the variation of the composition of o-phase and m-phase differs for HZO grown on MgO(100) and Al_2O_3(11–20) substrates with a Pt seed layer. This indicates that the strain is also an important factor for the high-quality growth of o-phase HZO.

To demonstrate the ferroelectric properties of the orthorhombic phase HZO film, piezoresponse force microscopy (PFM) results are shown in Fig. 5. HZO and HfO_2 films were both prepared at the optimized growth conditions of 600 °C with a thickness of 20 nm. Figures 5(a) and 5(b) show the morphology image of the region where the voltage is applied at the as-grown state (a) and after applying poling voltages (b). Figures 5(c) and 5(d) show the phase change before and after applying polishing voltages. The phase change of about 180° is observed after applying ±5 V voltage inside the selected regions. To demonstrate the uniformity of the ferroelectricity, phase [Fig. 5(e)] and amplitude [Fig. 5(f)] of four selected points in the selected regions are shown as a function of applied electric field, and

clear ferroelectric switching is observed, consistent with Figs. 5(c) and 5(d). Figures 5(i) and 5(j) show the comparison of the phase (i) and amplitude (j) signals of the remanent PFM hysteresis loop of the functional layer HZO and HfO_2 films. These two films have a similar structure of functional layers/Pt/substrates as indicated in Fig. 5. It can be seen that HZO films (red line) exhibit steeper phase reversal than HfO_2 (dark line) near the coercive voltages, which may indicate improved ferroelectric properties of the thin film after the introduction of Zr by HfO_2 [Fig. 5(i)]. Figure 5(j) shows that the butterfly curve of HZO and HfO_2 films, in which the HZO films have better properties with symmetry, verifies that the ferroelectric performance of HZO thin films better after introducing the seed layer, which is significantly improved due to the improvement of the o-phase. The amplitude of HZO is also about twice that of HfO_2 films. In addition, we measured the voltage-dependent polarization curve (PE loop) for the HZO/Pt/substrate structure, as shown in Fig. 5(k). The results indicate that the PE curves nearly saturate at large fields with slight drops, primarily due to the relatively high leakage current of the film, which causes the actual voltage applied to the film to be lower than the voltage displayed by the ferroelectric analyzer, preventing the film from reaching its saturation voltage.

In order to reveal the dynamical mechanisms of the orthorhombic and monoclinic phases of HfO_2 and HZO films, we calculated the surface potential energy and nuclear potential energy of HZO along different directions in Fig. 6. Figures 6(a) and 6(b) show the two different structures of the orthorhombic and monoclinic phases of HZO. Figures 6(c) and 6(d) show the calculated surface energy as well as the nucleation energy for two different HZO phases with different orientations. It can be seen that both the nucleation energy and surface energy required to form (111)-oriented HZO are significantly low for both orthorhombic and monoclinic phases. Remarkably, the nucleation energy of the orthorhombic
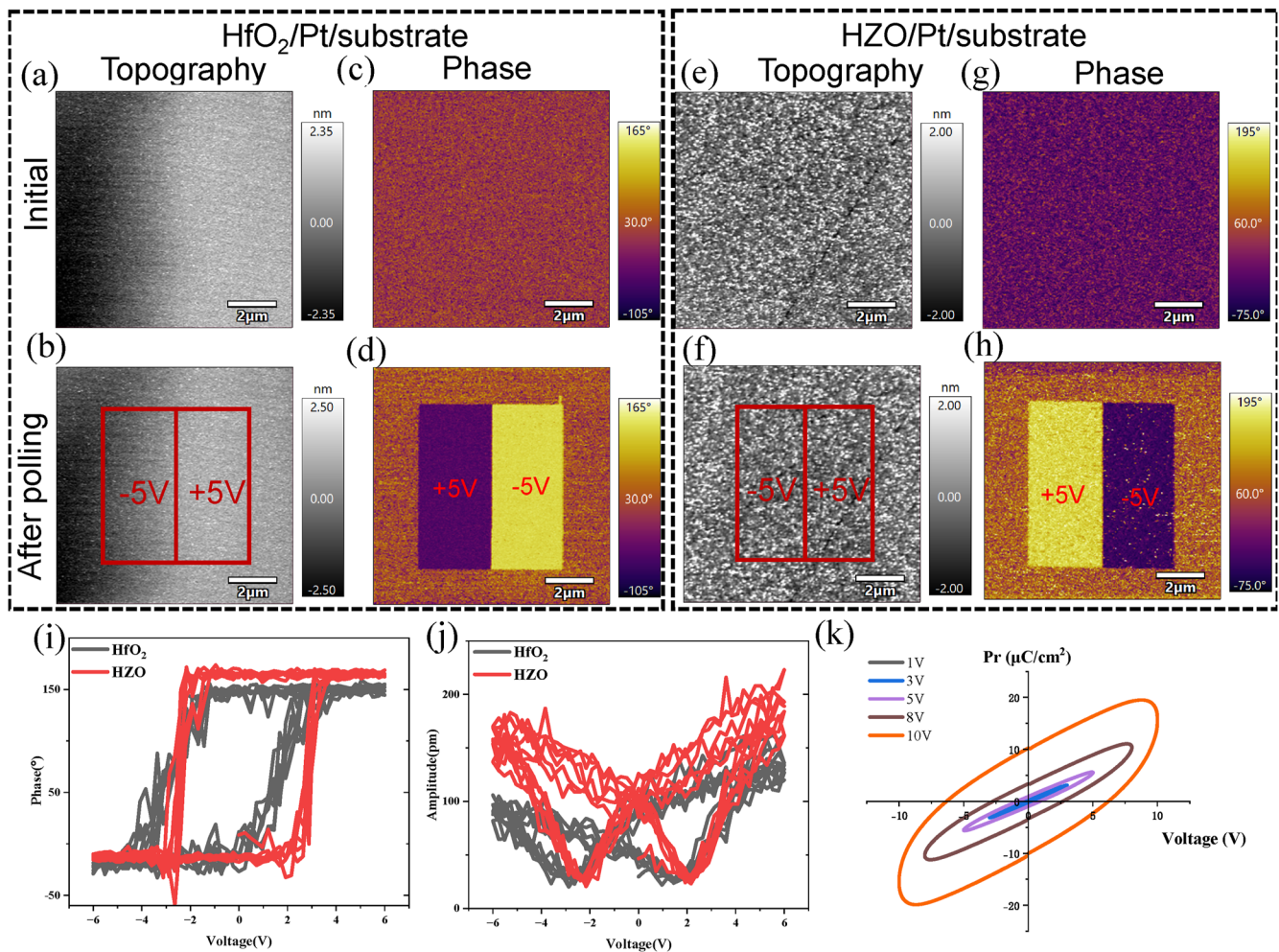
FIG. 5. Out-of-plane polarization switching and PFM hysteresis loops of HfO$_2$ and HZO thin films on Pt seed layer, as well as ferroelectric polarization curve of 10 nm HZO thin film. (a)–(d) PFM topography (a) and (b) and phase (c) and (d) contrasts of HfO$_2$ film with switchable out-of-plane polarizations before (a) and (c) and after electric poling (b) and (d) by applying +5 V (left) and −5 V (right) tip biases within the area enclosed by the red rectangles. (e)–(h) PFM topography (e) and (f) and phase (g) and (h) contrasts of HZO film with switchable out-of-plane polarizations before (e) and (f) and after electric poling (g) and (h) by applying +5 V (left) and −5 V (right) tip biases within the area enclosed by the red rectangles. (i) and (j) Comparison of phase (i) and amplitude (j) signals of HfO$_2$ and HZO remnant hysteresis loops. The red lines are from HZO, and the black lines are from HfO$_2$. The thicknesses of both samples are 20 nm and were grown at 600 °C. (k) Polarization as a function of voltage (PE loop) of a 10 nm HZO/Pt/substrate sample with different voltage ranges.

phase in (111)-oriented HZO is lower than that of the monoclinic phase. This indicates that it is preferable to stabilize the orthorhombic phase in (111)-oriented HZO, which is fully consistent with our experimental results shown in Fig. 6. Note that the seed layer Pt we introduced is with a (111)-oriented face-centered cubic structure; therefore, monoclinic HfO$_2$ is formed, which has a peak at 28.5° of m(−111) in XRD. The HZO film with a (111)-oriented seed Pt layer successfully stabilizes at the orthorhombic phase with a favored orientation along (111) [Figs. 6(e)–6(g)]. Several studies have explored the influence of stress on the orientation of HZO by introducing seed layers with varying orientations,[15] a result that aligns with our conclusions. The strain effect is crucial for the formation of ferroelectric o-phase HZO, especially along the (111)

direction. This observation aligns with the thickness-dependent ratio of the o-phase to m-phase in HZO, as depicted in Figs. 6(h) and 6(i). Specifically, Figs. 6(h) and 6(i) present the variation in the o-phase to m-phase ratio for HZO films of different thicknesses grown on three distinct substrates. Based on the area ratio [Fig. 6(h), determined from the integrated peak areas in the XRD data for the o-phase and m-phase] and the intensity ratio [Fig. 6(i), derived from the relative peak intensities in the XRD data], it can be concluded that the proportion of the o-phase exhibits a pronounced inverse correlation with film thickness. Furthermore, it is evident that the o-phase grows preferentially on MgO substrates compared to the silicon and sapphire substrates. In summary, the formation of the o-phase is governed by a combination of factors, including strain,
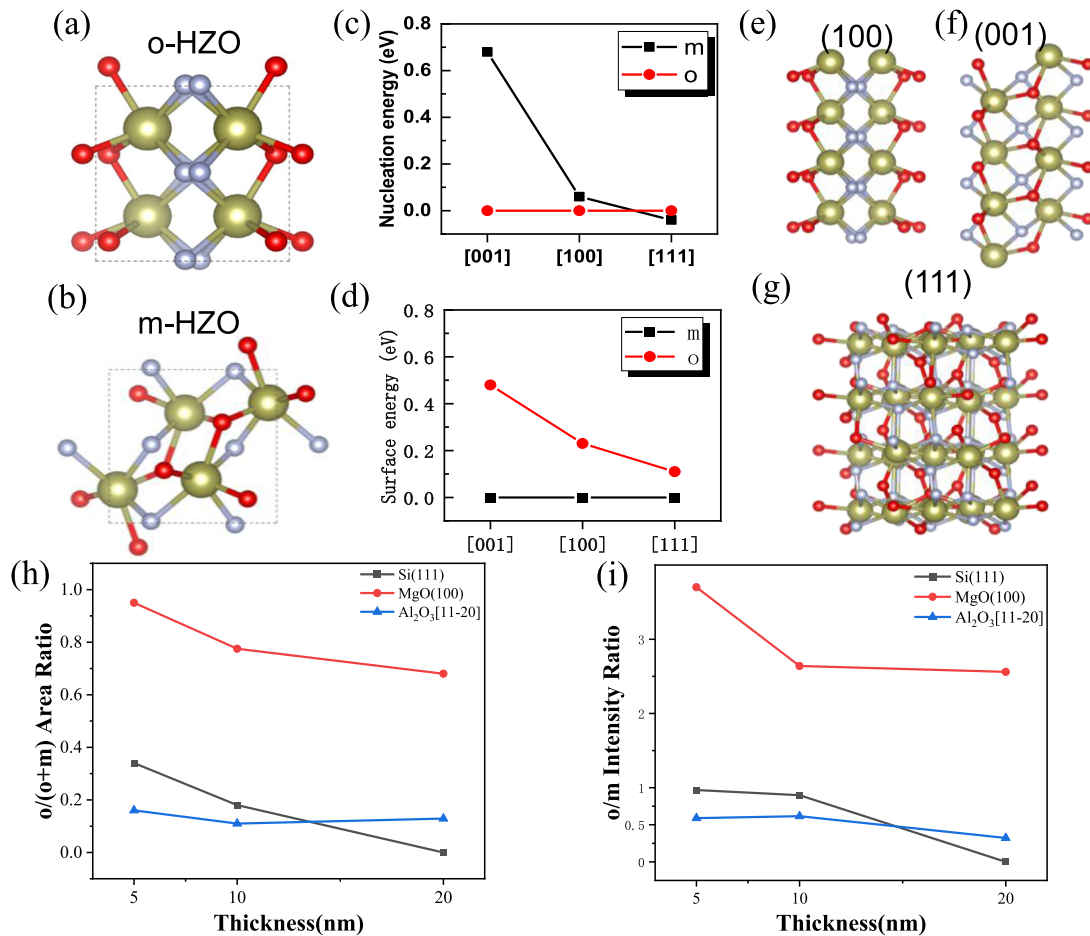
FIG. 6. Dynamical growth mechanism of orthorhombic HZO film. (a) and (b) Crystal structures of orthorhombic phase (a) and monoclinic phase (b) HZO. (c) Nucleation energy of monoclinic and orthorhombic phases HZO along different directions. (d) Surface energy of monoclinic and orthorhombic phases HZO along different directions. Atomic crystal structures of orthorhombic phase HZO along different directions (001) (e), (001) (f), and (111) (g). (h) The ratio of the area of the o/o + m phase in HZO thin films of different thicknesses. (i) The intensity ratio of the o/m peak in XRD.

formation energy, nucleation energy, and the relaxation of lattice strain.

To analyze the growth of HZO o-phase, two primary factors play a key role. First, the crystal phase and the orientation play a crucial role. Among the various orientations of HZO, the o-(111) orientation emerges as the main contributor to HZO's ferroelectric performance. Achieving crystal phase matching leads to superior-quality epitaxial films.[32,37,38] In this experiment, our focus was on this specific (111)-orientation, prompting the selection of a Pt(111) seed layer with a matching orientation. We attribute the seed layer's ability to induce o-phase HZO growth to Pt's face-centered cubic structure, where the (111)-orientation boasts the highest density. Consequently, o-(111) HZO crystals exhibit a preference for stable growth on Pt(111) surfaces. Second, strain plays a significant role. One major source of strain arises from the stress between the growing HZO layer and the underlying layers, a result of the lattice constant mismatch between the substrate and HZO. Inserting

a Pt buffer layer mitigates this lattice constant difference, enhancing lattice matching and promoting HZO growth. Another aspect of strain arises from variations in thermal expansion coefficients in the growth and cooling procedures. In physical vapor deposition, the heating and cooling process unfolds gradually. During this extended process, the change in temperature leads to fluctuations in the thermal expansion coefficients of HZO films and Pt, as well as sapphire or MgO substrates. A smaller thermal expansion coefficient favors the growth of m-phase HZO films.[39,40] Consequently, we opt to grow HZO films at higher temperatures to increase the thermal expansion coefficient. The difference in the thermal expansion, especially in the cooling process, would lead to different strain conditions, resulting in different contents of o-phase and m-phase (Figs. 5 and S3).

In conclusion, we have demonstrated stabilization of the polar orthorhombic HZO phase using a simple lattice and crystal structure matched to be bottom electrode Pt(111). XRD, high resolution STEM images, and SAD patterns of HZO films directly show the

high quality of the films. Thermodynamic calculations reveal the critical role of orientation-dependent nucleation energy and surface energy in stabilizing the orthorhombic phase over the monoclinic phase. This provides us an approach to selectively grow the ferroelectric HZO films, which is readily available for the integration of ferroelectric transistors.

EXPERIMENTAL METHODS

Sample preparation

A Platinum (Pt) seed layer was grown on commercial MgO(100) and sapphire substrates by sputtering in an Ar atmosphere under 0.30 Pa with a power of 50 W, and $Hf_{0.5}Zr_{0.5}O_2$(HZO) was then grown by sputtering at a growth temperature of 600 °C in an Ar atmosphere under 1.30 Pa with a power of RF 100 W. After deposition of Pt and HZO, the sample was maintained at 600 °C for ten minutes, then cooled to room temperature at a rate of 10 °C/min in an Ar atmosphere.

X-ray diffraction (XRD)

This experiment utilized X-ray diffraction (XRD) for characterization purposes, and the machine we used is the D8 ADVANCE. During θ–2θ testing, the sample is first placed on the instrument's sample stage, ensuring a specific angle relationship between the sample and the x-ray beam. Then, the incidence angle θ is incrementally changed, and the diffraction intensity at each 2θ angle under different θ values is recorded.

X-ray reflectivity (XRR)

X-ray Reflectivity (XRR) testing involves irradiating the sample surface with a monochromatic x-ray beam and observing the reflected x-ray intensity at different angles within a certain range. These angle variations provide detailed information about the surface morphology and layer structure of the sample. By analyzing the relationship between the reflected intensity and the incident angle using the Huber five-circle diffractometer in the 1W1A-Diffuse Scattering Experimental Station, one can obtain information about the thickness of each layer, interface roughness, and the interfacial structure between layers in the sample. Simulation of XRR data was performed on https://henke.lbl.gov/optical_constants/bilayer.html.

Piezoresponse force microscopy (PFM) measurements

A commercial scanning probe microscopy system was used to perform the PFM measurements. The conducting substrate of HZO was grounded during the measurements. An AC bias with an amplitude of 0.5–1 V was applied to the film via a conductive Pt-coated Si tip. A resonance enhancement mode (Dual AC Resonance Tracking) was used to amplify the piezoresponse signal. The typical drive frequency was in the range of 320–360 kHz, and the typical loading force for the PFM scan was in the range of 20–40 nN, which did not damage the film surface during the PFM imaging. The switching spectroscopy-PFM (SS-PFM) technique was used to acquire the ferroelectric hysteresis loops from the HZO membranes. A typical triangular-square DC pulse train embedded with a detection AC bias was applied. The remanent piezoresponse (i.e., when DC bias = 0) was used to plot the hysteresis loops. The amplitude loop reveals the strain hysteresis, while the phase loop demonstrates the polarization switching process with an about 180° phase change.

Transmission electron microscopy (TEM) characterization

The cross section TEM sample of HZO was prepared by a dual beam Thermo Fisher Scientific dual beam "Scios 2 HiVac" system. The notches were prepared at an acceleration voltage of 30 kV using Ga ions to 100 nm with a voltage of 30 kV from 2 μm, followed by surface cleaning with a voltage of 5 and 2 kV. An FEI Talos F200X transmission electron microscope (TEM) was operated during the characterization at 200 kV. The electron beam current was set to 30 pA in high-angle annular dark field (HAADF) mode for image recording with a convergence angle of 50 mrad.

DFT calculation

The first-principles calculations were performed by density functional theory on the basis of the projector-augmented wave method as implemented in the VASP code.[12] The Perdew–Burke–Ernzerhof (PBE) functional within the generalized gradient approximation (GGA) was used to describe the exchange-correlation interaction.[3] The plane-wave basis cutoff energy was set to be 400 eV. The Monkhorst–Pack k-point mesh was sampled with a separation of about 0.015 Å in the Brillouin zone. All structures were relaxed until the residual atomic force and total energy fluctuation were less than 0.01 eV/Å and 10^{-5} eV, respectively.

Here, orthorhombic (o, Pbca) and monoclinic (m, P2$_1$/c) phases of HfZrO$_2$ (HZO) were employed to construct the HZO surface. The surface energy (E_S) was calculated by the following equation:

$$E_S = \frac{1}{4A}\left(E_{slab1} + E_{slab2} - 2E_{bulk}\right),$$

where the 4A is the surface area of the four surfaces of the two created symmetric slabs, E_{slab1} and E_{slab2} are the total energies of two HZO slabs that formed by splitting the HZO bulk, and E_{bulk} is the total energy of the HZO bulk.

The crystal nucleus models were constituted of one Hf–O enneahedron and one Zr–O enneahedron on the Si(111) surface. Therefore, the nucleation energy was calculated by the following equation:

$$E_n = E_{nucleus} - E_{Si} - n_{Hf}E_{Hf} - n_{Zr}E_{Zr} - n_OE_O,$$

where $E_{nucleus}$ and E_{Si} are total energies of the crystal nucleus model and Si(111) surface, respectively, E_{Hf}, E_{Zr}, and E_O are the energies of the Hf, Zr, and O elements, respectively, and n_{Hf}, n_{Zr}, and n_O are the numbers of Hf, Zr, and O atoms in the crystal nucleus model, respectively.[41-43]

SUPPLEMENTARY MATERIAL

The supplementary material includes details of temperature-dependent samples and related data.

AUTHOR DECLARATIONS

Conflict of Interest

The authors have no conflicts to disclose.

Author Contributions

Jiang Zhu: Conceptualization (lead); Data curation (lead); Formal analysis (lead); Investigation (lead); Methodology (equal); Resources (lead); Supervision (lead); Writing – original draft (lead); Writing – review & editing (lead). **Yongyi Wu**: Formal analysis (equal); Methodology (equal); Software (equal). **Hao-Nan Li**: Project administration (equal); Validation (equal). **Lei Wang**: Resources (equal); Supervision (equal). **Yue-Qi Wang**: Funding acquisition (equal); Project administration (equal). **Xian-Qin Liu**: Data curation (equal). **Yi-Xing He**: Formal analysis (equal); Resources (equal). **Siwen Zhang**: Data curation (equal). **Jie Su**: Methodology (equal); Validation (equal). **Tao Li**: Formal analysis (equal). **Haijiao Harsan Ma**: Data curation (equal); Funding acquisition (equal); Investigation (equal); Project administration (equal); Supervision (equal). **Jincheng Zhang**: Data curation (equal); Methodology (equal). **Yue Hao**: Project administration (equal); Supervision (equal).

DATA AVAILABILITY

The data that support the findings of this study are available within the article and its supplementary material.

REFERENCES

[1] E. Yurchuk et al., "Charge-trapping phenomena in HfO$_2$-based FeFET-type nonvolatile memories," IEEE Trans. Electron Devices **63**(9), 3501–3507 (2016).

[2] K. Toprasertpong, M. Takenaka, and S. Takagi, "Direct observation of interface charge behaviors in FeFET by quasi-static split C–V and Hall techniques: Revealing FeFET operation," in *2019 IEEE International Electron Devices Meeting (IEDM)* (IEEE, San Francisco, CA, 2019), pp. 23.7.1–23.7.4.

[3] S. Dünkel et al., "A FeFET based super-low-power ultra-fast embedded NVM technology for 22 nm FDSOI and beyond," in *2017 IEEE International Electron Devices Meeting (IEDM)* (IEEE, San Francisco, CA, 2017), pp. 19.7.1–19.7.4.

[4] H. Y. Yoong, H. Wu, J. Zhao, H. Wang, R. Guo, J. Xiao, B. Zhang, P. Yang, S. J. Pennycook, N. Deng, X. Yan, and J. Chen, Adv. Funct. Mater. **28**, 1806037 (2018).

[5] A. I. Khan, A. Keshavarzi, and S. Datta, "The future of ferroelectric field-effect transistor technology," Nat. Electron. **3**(10), 588–597 (2020).

[6] Z. Liang et al., "A novel high-endurance FeFET memory device based on ZrO$_2$ anti-ferroelectric and IGZO channel," in *2021 IEEE International Electron Devices Meeting (IEDM)* (IEEE, San Francisco, CA, 2021), pp. 17.3.1–17.3.4.

[7] T. Cui et al., "Can interface layer be really free for Hf$_x$Zr$_{1-x}$O$_2$ based ferroelectric field-effect transistors with oxide semiconductor channel?," IEEE Electron Device Lett. **45**(3), 368–371 (2024).

[8] B. Y. Kim, B. S. Kim, S. D. Hyun, H. H. Kim, Y. B. Lee, H. W. Park, M. H. Park, and C. S. Hwang, "Study of ferroelectric characteristics of Hf$_{0.5}$Zr$_{0.5}$O$_2$ thin films grown on sputtered or atomic-layer-deposited TiN bottom electrodes," Appl. Phys. Lett. **117**(2), 022902 (2020).

[9] Q. Luo et al., "Composition-dependent ferroelectric properties in sputtered Hf$_x$Zr$_{1-x}$O$_2$ thin films," IEEE Electron Device Lett. **40**(4), 570–573 (2019).

[10] Y.-K. Liang et al., "Demonstration of highly robust 5 nm Hf$_{0.5}$Zr$_{0.5}$O$_2$ ultra-thin ferroelectric capacitor by improving interface quality," IEEE Electron Device Lett. **42**(9), 1299–1302 (2021).

[11] T. S. Böscke, J. Müller, D. Bräuhaus, U. Schröder, and U. Böttger, "Ferroelectricity in hafnium oxide thin films," Appl. Phys. Lett. **99**(10), 102903 (2011).

[12] S. Lee, Y. C. Jung, H. R. Park et al., "Analysis of ferroelectric properties of ALD-Hf$_{0.5}$Zr$_{0.5}$O$_2$ thin films according to oxygen sources," Solid-State Electron. **216**, 108911 (2024).

[13] S. J. Kim, J. Mohan, S. R. Summerfelt, and J. Kim, "Ferroelectric Hf$_{0.5}$Zr$_{0.5}$O$_2$ thin films: A review of recent advances," JOM **71**, 246–255 (2019).

[14] H. Kim, A. Kashir, S. Oh et al., "Effects of high pressure oxygen annealing on Hf$_{0.5}$Zr$_{0.5}$O$_2$ ferroelectric device," Nanotechnology **32**(31), 315712 (2021).

[15] J. W. Cho, M. S. Song, I. H. Choi et al., "Atomic layer deposition of epitaxial ferroelectric Hf$_{0.5}$Zr$_{0.5}$O$_2$ thin films," Adv. Funct. Mater. **34**, 2314396 (2024).

[16] C. Han et al., "Effects of RTA rising time on ferroelectric characteristics of HfZrO$_2$," IEEE Trans. Electron Devices **69**(6), 3499–3502 (2022).

[17] B. Zhao, Y. Yan, J. Bi, G. Xu, Y. Xu, X. Yang, L. Fan, and M. Liu, "Improved ferroelectric properties in Hf$_{0.5}$Zr$_{0.5}$O$_2$ thin films by microwave annealing," Nanomaterials **12**, 3001 (2022).

[18] F. Huang, B. Saini, L. Wan et al., "Dimensional scaling of ferroelectric properties of hafnia-zirconia thin films: Electrode interface effects," ACS Nano **18**(27), 17600–17610 (2024).

[19] Y.-H. Chen, C.-J. Su, C. Hu, and T.-L. Wu, "Effects of annealing on ferroelectric hafnium–zirconium–oxide-based transistor technology," IEEE Electron Device Lett. **40**(3), 467–470 (2019).

[20] T. Song, S. Estandía, H. Tan, N. Dix, J. Gàzquez, I. Fina, and F. Sánchez, "Positive effect of parasitic monoclinic phase of Hf$_{0.5}$Zr$_{0.5}$O$_2$ on ferroelectric endurance," Adv. Electron. Mater. **8**, 2100420 (2022).

[21] T. Kiguchi, S. Nakamura, A. Akama et al., "Solid state epitaxy of (Hf, Zr) O$_2$ thin films with orthorhombic phase," J. Ceram. Soc. Jpn. **124**(6), 689–693 (2016).

[22] T. Song, F. Sánchez, and I. Fina, "Impact of non-ferroelectric phases on switching dynamics in epitaxial ferroelectric Hf$_{0.5}$Zr$_{0.5}$O$_2$ films," APL Mater. **10**(3), 031108 (2022).

[23] H. A. Hsain, P. Sharma, H. Yu et al., "Enhanced piezoelectricity of thin film hafnia-zirconia (HZO) by inorganic flexible substrates," Appl. Phys. Lett. **113**(2), 022905 (2018).

[24] H.-K. Peng, C.-Y. Chiu, Y.-C. Kao, P.-J. Wu, and Y.-H. Wu, "Enhanced reliability, switching speed and uniformity for ferroelectric HfZrO$_x$ on epitaxial Ge film by post deposition annealing for oxygen vacancy control," IEEE Trans. Electron Devices **69**(7), 4002–4009 (2022).

[25] J. Aarik, A. Aidla, A. A. Kiisler et al., "Influence of substrate temperature on atomic layer growth and properties of HfO$_2$ thin films," Thin Solid Films **340**(1–2), 110–116 (1999).

[26] D. Triyoso, R. Liu, D. Roan et al., "Impact of deposition and annealing temperature on material and electrical characteristics of ALD HfO$_2$," J. Electrochem. Soc. **151**(10), F220 (2004).

[27] M. H. Park, C. C. Chung, T. Schenk et al., "Effect of annealing ferroelectric HfO$_2$ thin films: In situ, high temperature x-ray diffraction," Adv. Electron. Mater. **4**(7), 1800091 (2018).

[28] J. Lee, S. H. Kim, H. Choi et al., "Ferroelectricity of $Hf_{0.5}Zr_{0.5}O_2$ thin film induced at $350\,^\circ C$ by thermally accelerated nucleation during atomic layer deposition," IEEE Trans. Electron Devices **71**(4), 2690–2695 (2024).

[29] F. Huang, B. Saini, Z. Yu et al., "Enhanced switching reliability of $Hf_{0.5}Zr_{0.5}O_2$ ferroelectric films induced by interface engineering," ACS Appl. Mater. Interfaces **15**(43), 50246–50253 (2023).

[30] A. Miakonkikh, A. Lomov, A. Rogozhin et al., "Phase transformation in ALD hafnia based layers for silicon-on-ferroelectric devices," in *2020 Joint International EUROSOI Workshop and International Conference on Ultimate Integration on Silicon (EUROSOI-ULIS)* (IEEE, 2020), pp. 1–4.

[31] S. Kumari, N. Mottaghi, C. Y. Huang et al., "Effects of oxygen modification on the structural and magnetic properties of highly epitaxial $La_{0.7}Sr_{0.3}MnO_3$ (LSMO) thin films," Sci. Rep. **10**(1), 3659 (2020).

[32] H. Tan, T. Song, N. Dix et al., "Vector piezoelectric response and ferroelectric domain formation in $Hf_{0.5}Zr_{0.5}O_2$ films," J. Mater. Chem. C **11**(22), 7219–7226 (2023).

[33] H. Tan, A. Quintana, N. Dix et al., "Photovoltaic-driven dual optical writing and non-destructive voltage-less reading of polarization in ferroelectric $Hf_{0.5}Zr_{0.5}O_2$ for energy efficient memory devices," Nano Energy **123**, 109384 (2024).

[34] S. Estandía, J. Gazquez, M. Varela et al., "Critical effect of the bottom electrode on the ferroelectricity of epitaxial $Hf_{0.5}Zr_{0.5}O_2$ thin films," J. Mater. Chem. C **9**(10), 3486–3492 (2021).

[35] M. B. Hachemi, B. Salem, V. Consonni et al., "Study of structural and electrical properties of ferroelectric HZO films obtained by single-target sputtering," AIP Adv. **11**(8), 085004 (2021).

[36] S. Shi, H. Xi, T. Cao et al., "Interface-engineered ferroelectricity of epitaxial $Hf_{0.5}Zr_{0.5}O_2$ thin films," Nat. Commun. **14**(1), 1780 (2023).

[37] S. Estandía et al., "Domain-matching epitaxy of ferroelectric $Hf_{0.5}Zr_{0.5}O_2$ (111) on $La_{2/3}Sr_{1/3}MnO_3$ (001)," Cryst. Growth Des. **20**(6), 3801–3806 (2020).

[38] Y. Goh, S. H. Cho, S.-H. K. Park, and S. Jeon, "Crystalline phase-controlled high-quality hafnia ferroelectric with RuO_2 electrode," IEEE Trans. Electron Devices **67**(8), 3431–3434 (2020).

[39] Y. Goh, J. Hwang, Y. Lee, M. Kim, and S. Jeon, "Ultra-thin $Hf_{0.5}Zr_{0.5}O_2$ thin-film-based ferroelectric tunnel junction via stress induced crystallization," Appl. Phys. Lett. **117**(24), 242901 (2020).

[40] Y.-T. Tsai et al., "Physical insights of low thermal expansion coefficient electrode stress effect on hafnia-based switching speed," arXiv:2307.04404 (2023).

[41] W. Kohn and L. J. Sham, "Self-consistent equations including exchange and correlation effects," Phys. Rev. **140**(4A), A1133–A1138 (1965).

[42] P. E. Bloechl, "Projector augmented-wave method," Phys. Rev. B **50**, 17953–17979 (1994).

[43] J. P. Perdew, K. Burke, and M. Ernzerhof, "Generalized gradient approximation made simple," Phys. Rev. Lett. **77**(18), 3865–3868 (1996).